In situ real-time monitoring of profile evolution during plasma etching of mesoporous low-dielectric-constant SiO_2

Henry Gerung, C. Jeffrey Brinker, Steven R. J. Brueck, and Sang M. Han[a)]
University of New Mexico, Albuquerque, New Mexico 87131

(Received 21 June 2004; accepted 3 January 2005; published 1 March 2005)

We have employed attenuated total reflection Fourier transforms infrared spectroscopy (ATR-FTIRS) to monitor the profile evolution of patterned mesoporous, low-dielectric-constant SiO_2 films *in situ* and in real time during plasma etching. A stack of patterned photoresist, anti-reflective coating, and mesoporous SiO_2 is etched in an inductively coupled plasma reactor, using CHF_3 and Ar. During etching, the IR absorbance of Si–O–Si stretching modes near 1080 cm^{-1} decreases, and the rate of decrease in Si–O–Si absorbance translates to the SiO_2 removal rate. When corrected for the exponentially decaying evanescent electric field, the removal rate helps monitor the profile evolution and predict the final etch profile. The predicted profiles are in excellent agreement with the cross-sectional images taken by scanning electron microscopy. In a similar approach, we calculate the absolute total number of C–F bonds in the sidewall passivation and observe its formation rate as a function of time. Assuming that the thickness of the sidewall passivation tapers down towards the trench bottom, we deduce that C–F formation occurs mostly in the final stage of etching when the trench bottom meets the Ge ATR crystal and that a critical amount of C–F buildup is necessary to maintain the anisotropic etch profile. © *2005 American Vacuum Society.*
[DOI: 10.1116/1.1865154]

I. INTRODUCTION

The integrated circuit (IC) manufacturing has witnessed continuous device miniaturization giving rise to numerous engineering challenges. According to the 2003 International Technology Roadmap for Semiconductors (ITRS), the IC device dimension will reach an 18 nm node by 2018.[1] For advanced microprocessors and logic devices, in particular, such miniaturization requires a reduction in the resistance-capacitance (RC) time constant associated with metal interconnects and intermetal dielectrics.[2] The purpose is to increase the device operating speed despite the miniaturization. Two primary solutions exist today to reduce the RC constant. One is copper metallization, and the other is low-dielectric-constant materials insulating the metal interconnects. A variety of materials, such as polytetrafluoro ethylene (PTFE),[3,4] polyimides (PI),[5–7] silsesquioxanes,[8] and mesoporous SiO_2,[9] have been considered as viable candidates to replace the conventional vapor-deposition-based SiO_2. In this study, we focus on solgel-based mesoporous SiO_2 whose dielectric constant ranges from 1.5 to 2.0 in the 1–40 GHz range.[10] We demonstrate that the patterned etch profile of SiO_2 film, along with the sidewall passivation, can be monitored *in situ* and in real time, using attenuated total reflection Fourier transform infrared spectroscopy (ATR-FTIRS). The ATR technique has been previously used to study surface reactions during plasma enhanced processes[11–14] as well as "resetting" the wall condition of commercial plasma reactors for process reproducibility.[15] In all cases, the ATR technique provides sub-monolayer sensitivity to examine heterogeneous reactions occurring on semiconductor and insulator films.[16,17] We take advantage of the high sensitivity to probe the patterned surface of mesoporous SiO_2 films during etching. This nondestructive method eliminates the need for cross-sectional scanning electron microscopy (XSEM) to examine the etch profile. We expect that the ATR-FTIRS technique and our analytical approach can be applied to other dielectric films such as Si_3N_4 and SiO_xN_y during etching for the purpose of process development. The wafer-level use of the ATR technique in production tools, however, might be limiting, since the multilevel, intermetal dielectric architecture contains metal interconnects. These metal lines, whose pitch is smaller than the wavelength of IR, would prevent the evanescent wave from propagating through the dielectric film.

II. EXPERIMENT

Figure 1 illustrates a top cross-sectional view of our experimental setup. The stainless steel, tubular plasma chamber is 25 cm in diameter with multiple view ports. A turbomolecular pump (Alcatel 5900CP) with 1000 l/s pumping speed maintains the base pressure at 6.7×10^{-4} Pa. The turbomolecular pump is assisted by a 14 l/s double-stage rotary vane mechanical pump (Edwards E2M40). A gate valve controls the conductance to the turbomolecular pump and maintains the chamber pressure at 1.3 Pa during etching, independent of reactant gas flow rates. A mixture of CHF_3 and Ar is introduced to the chamber through a 10 cm diam circular gas distribution ring located 12.5 cm above the substrate. During etching, mass flow controllers (UNIT URS 100-5) maintain the flow rates of CHF_3 and Ar constant.

A "stove-top-coil" inductive plasma source is mounted on a 2.54 cm thick, 16 cm diam Pyrex window that separates the plasma source from vacuum. A radio frequency (rf) potential

[a)]Electronic mail: meister@unm.edu

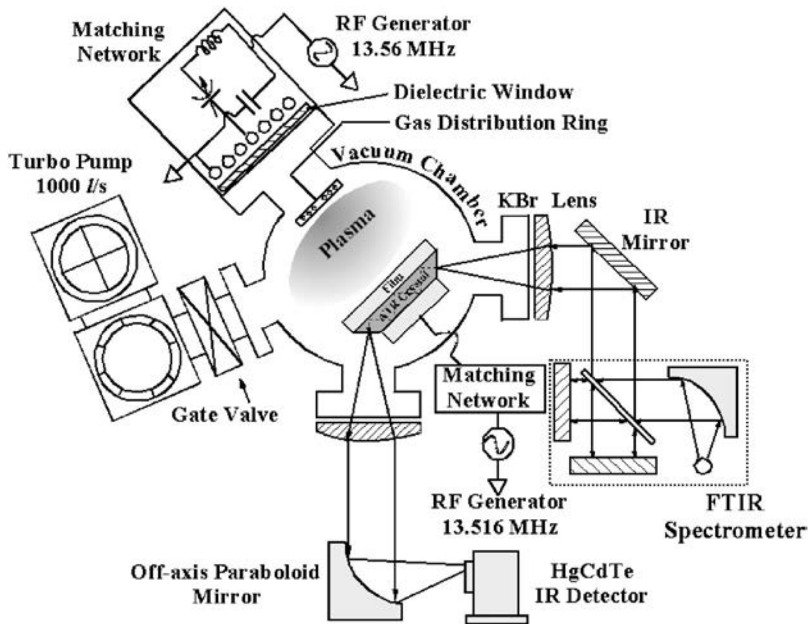

FIG. 1. Schematic diagram of plasma etch chamber equipped with ATR-FTIRS setup.

at 13.56 MHz is applied to the plasma source through an impedance matching network to maximize the power delivery to the plasma. An independent rf potential at 13.516 MHz is applied to the substrate holder to control the ion energy.[18–21] The slight frequency offset from 13.56 MHz is meant to avoid interference with the plasma source frequency. The rf power delivered to the plasma source is maintained at 400–800 W, while the rf power delivered to the substrate is maintained at 100–150 W. Although the reactor geometry departs from commercial reactors, we expect the plasma conditions (e.g., density of reactive neutrals and ions, ion energy distribution, and ion angular distribution) to be comparable to those of commercial reactors based on the aforementioned rf power consumption and independent bias.

For ATR-FTIRS, a trapezoidally shaped Ge(111) crystal is mounted on a metal substrate platen cooled by chilled water. The choice of the ATR substrate (e.g., GaAs and KRS-5) is immaterial, provided that the substrate is IR-transparent in the mid-IR region. We also expect the effect of the substrate on etch chemistry to be minimal prior to the endpoint, since reactive radicals and energetic ions impinge almost entirely on the film surface rather than on the underlying ATR substrate during etching. Figure 2 illustrates that the Ge crystal is coated with mesoporous SiO_2, anti-reflective coating (ARC), and fully patterned photoresist (PR). The patterned PR serves as an etch mask. The preparation steps for these films will be discussed in the following section.

The Ge crystal is 5 cm long, 2 cm wide, and 2 mm thick with two ends beveled at 45° with respect to the substrate normal. The IR beam from a FTIR spectrometer (Nicolet Nexus 670) is focused onto a beveled edge. Upon entering the crystal, the IR beam undergoes ~12 reflections from the crystal top surface and exits the opposite beveled edge. The above arrangement renders the Ge crystal transparent to IR above 650 cm^{-1}. The multiple internal reflections also significantly enhance the IR absorption that stems from the changes in the film on top of the ATR substrate, especially in comparison to the IR absorption that stems from the changes on the beveled edges. In addition, the flat crystal surface area is ~10 times greater than that of the two beveled edges. Note also that the beveled edges face away from the plasma source and that the oxide film, deposited on the longer side of the ATR crystal, faces the plasma source (Figs. 1 and 2). These factors ensure that the absorption signal from the film is at least two orders of magnitude greater than that from the beveled edges. The ATR technique is also robust against scratches inadvertently introduced during sample transfer to and from the plasma chamber. We have previously demonstrated that the surface corrugation, whether introduced natu-

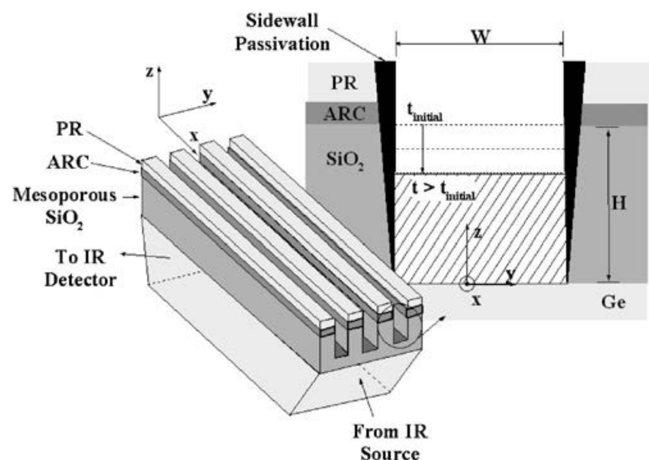

FIG. 2. Conceptual layout of a partially patterned SiO_2 film on a Ge ATR crystal. The ATR technique is used to measure the removal rate of SiO_2 as well as the formation rate of C–F in the sidewall passivation layer. Patterned photoresist and anti-reflective coating are stacked on top of mesoporous SiO_2 film. The magnified cross-sectional view outlines the etch front at the trench bottom.

rally or artificially, does not cause IR to scatter upon internal reflection, provided that the corrugation dimension is less than the IR wavelength.[22]

The internal reflections create an evanescent electromagnetic field whose strength decays exponentially away from the film–crystal interface. Infrared-active dipole moments in the etched mesoporous SiO_2 film (e.g., C–F and Si–O–Si stretching vibrational modes) absorb the evanescent field at their characteristic vibrational frequencies. For instance, the IR absorbance peaks of C–F_x (x=1, 2, and 3) and Si–O–Si stretching vibrational modes appear at 1200–1700 and 890–1195 cm^{-1}, respectively.[14,23,24] Because the evanescent field strength decays exponentially away from the film–crystal interface, the IR absorption by dipole moments near the film–crystal interface is more pronounced than that away from the interface. The mathematical correction for the exponential decay will be described in Result and Discussion. The exiting IR is collimated by a KBr lens and then focused onto a HgCdTe mid-range IR detector by an off-axis paraboloid mirror. Prior to etching, a background spectrum is taken with 4 cm^{-1} resolution averaged over 50 scans. During etching, a series of sample spectra are collected with 4 cm^{-1} resolution. Each absorbance spectrum is averaged over 20 scans to maintain the peak-to-peak noise level below 0.016, while achieving the time resolution of 12 s.

Figure 2 depicts partially etched parallel trenches created in the mesoporous SiO_2 film during etching. The magnified view of a trench shows how PR, ARC, and mesoporous SiO_2 film are stacked on top of the Ge ATR crystal. To create this stack of films, the Ge crystal is first cleaned in 100% ethanol (EtOH) to dissolve organic contaminants on the surface. The substrate is then treated in air plasma for 2 min to increase the adhesion of a sol that contains SiO_2 film precursors. The sol consists of EtOH, H_2O, tetraethyl orthosilicate (TEOS), polyoxyethylene(10) cetyl ether (Brij 56), and a trace amount of HCl. We prepare the sol by a 2-step process before spin-coating it on the Ge crystal at 2000 rpm for 20 s. The first step is to create a stock solution (A2**) by mixing EtOH, H_2O, TEOS, and HCl at a molar ratio of 3.8: 1: 1: 5.1 $\times 10^{-5}$ and heating the solution at 333 K for 90 min. The purpose of heating is to expedite the hydrolysis of TEOS, replacing ethoxy groups with hydroxyl groups.[25] The second step is to dilute the prepared A2** stock solution with additional EtOH, H_2O, and HCl. Brij 56 is also added to set the molar composition of EtOH, H_2O, TEOS, Brij 56, and HCl at 20: 5: 1: 0.06: 4×10^{-3}. The HCl concentration is chosen to minimize premature condensation of TEOS while promoting the self-assembly of Brij 56 surfactant to form either a hexagonal or cubic phase template.[25] This template formation occurs concurrently with evaporation of EtOH and H_2O; hence, the template formation is named evaporation induced self-assembly (EISA).[26] The prepared sol is then spin-coated on the Ge crystal and allowed to dry in the ambient air (298 K and 30% relative humidity). The TEOS oligomers in the sol subsequently condense around the template upon calcining the spin-coated film in an oven filled with the ambient air. The oven temperature is ramped at 1 K/min to 673 K, maintained at this temperature for 180 min, and then cooled down to the room temperature (298 K) at the same rate. The removal of organic materials by calcination results in mesopores SiO_2 matrix. As control samples, we also prepare the mesoporous films on Si(100) under the same condition. These control samples are used to measure the etch rate and the post-etch profile, using XSEM. The SiO_2 film thickness is measured prior to coating ARC and PR, using variable-angle spectroscopic ellipsometry (Woolam WVASE32). The SiO_2 film thickness is ~2600 Å for all samples.

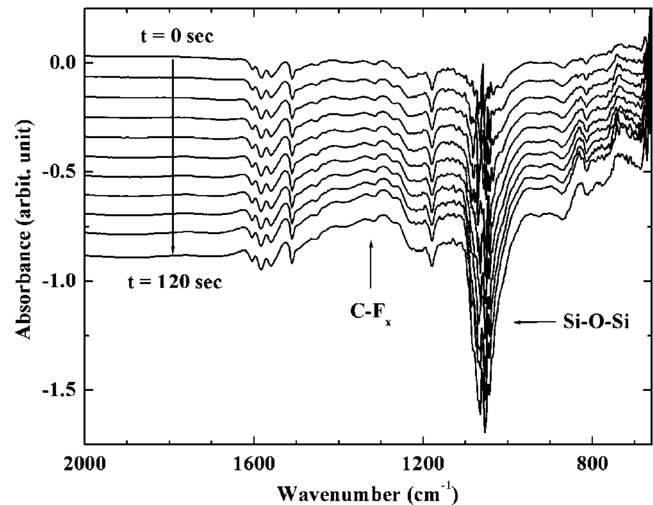

FIG. 3. Time-series of IR absorbance spectra taken during a 2 min etch process show both C–F and Si–O–Si stretching vibrational modes. Si–O–Si absorbance becomes increasingly negative, indicating its loss, whereas C–F absorbance becomes increasingly positive, indicating its gain during the etch.

The anti-reflective coating (Brewers Science XHRi-16) and photoresist (Shipley i300) are sequentially spin-coated on top of the SiO_2 film at 4000 rpm for 30 s. The thickness of ARC and PR is 1600 and 8000 Å, respectively. The photoresist is patterned by interferometric lithography (IL) described elsewhere.[27–30] The photoresist is exposed to the 355 nm line of a Nd:YaG laser operated at 55 mJ/pulse for 20 s, baked at 383 K, and then immersed in a developer solution (Shipley MF702) for 1 min. The pitch (P) and width (W) of the fully developed PR pattern are 0.3 and 0.15 μm, respectively. The underlying ARC is etched either in an O_2–Ar plasma or in a CHF_3–Ar plasma, depending on the desired etch profile. The O_2–Ar etch results in an anisotropic profile, whereas CHF_3–Ar plasma results in a profile where the mid-section bows out. The rf power delivered to the plasma source and substrate platen, pressure, and flow rates of O_2 and Ar are 100 W, 50 W, 1.3 Pa, 4 sccm, and 25 sccm, respectively.

III. RESULTS AND DISCUSSION

Figure 3 shows a typical set of time-series absorbance spectra taken during a 2 min etch to completely remove the exposed 2600 Å thick SiO_2 under the etch mask. The absorbance by Si–O–Si stretching vibrational modes from 890 to 1195 cm^{-1} decreases continuously in the negative direction

(Fig. 3). This observation is consistent with the fact that SiO_2 is removed during etching. The pronounced noise level near 1050 cm^{-1} is due to the fact that Si–O–Si stretching mode is a strong IR absorber and that the IR intensity of the reference background in the said region is minimal with a 2600 Å thick SiO_2 layer.

In contrast to the Si–O–Si absorbance, the absorbance by C–F_x vibrational modes near 1200–1700 cm^{-1} increases continuously, indicating that the total amount of fluorocarbon (FC) deposit increases throughout the etching process. This increase may stem from fluorocarbon accumulation on the sidewalls[31,32] and/or on the trench bottom. The work of Rueger *et al.*[33] and Standaert *et al.*,[34] using angle-resolved x-ray photoelectron spectroscopy (AR-XPS), demonstrates that a thin layer of FC exists on SiO_2 surfaces even under heavy ion bombardment. Thus, we expect the FC to exist both on the trench bottom as well as on the sidewalls. However, the heavy ion bombardment on an independently biased substrate is believed to maintain the FC accumulation at minimum.[33,35] The fluorocarbon would, therefore, accumulate mostly on the sidewalls.[32] In addition, the trench bottom area remains fairly constant throughout the etch, whereas the sidewall area continues to increase. Note also that we have discounted the FC deposit on trench tops from the possible cases discussed above. We have determined that the IR absorption contribution from the FC deposition on trench tops is minimal when the SiO_2 thickness is comparable to or significantly exceeds the depth of penetration of the evanescent wave. That is, when the FC deposit on trench top is placed outside or at a distance comparable to the probing depth of the evanescent wave, the observed IR absorption pertains to either the sidewalls or the trench bottom. Therefore, we deduce that the observed increase pertains mostly to the sidewalls.

Two mechanisms may contribute to the increase in fluorocarbon. (1) The fluorocarbon deposits in the sub-surface pores near the exposed SiO_2 sidewalls.[36] For porous SiO_2 with 2 nm wide pores and 30% porosity, similar to our mesoporous SiO_2, the sub-surface pore filling may reach a depth of ~3 to 4 nm.[36] As the etching exposes progressively increasing SiO_2 sidewall area with concurrent pore filling, the total amount of fluorocarbon increases; (2) the fluorocarbon deposits externally on top of the exposed SiO_2 sidewalls, and the total amount increases with increasing SiO_2 sidewall area. We assume that the rate of diffusion of fluorocarbon precursors through the mesopores (~2 nm) far exceeds the rate at which the exposed SiO_2 surface increases and that the precursor diffusion is self-limiting due to the fluorocarbon film sealing the mesopores.[32,36] Thus, we expect that the increase in C–F_x absorbance is primarily due to the FC build-up on top of the exposed SiO_2 sidewalls.

For a quantitative analysis to obtain the absolute amount of SiO_2 removal and C–F_x accumulation during etching, the IR absorbance spectra in Fig. 3 need to be corrected for the exponentially decaying evanescent field. A similar correction procedure has been previously described.[13,37] To summarize, we employ the effective thickness (d_e) approximation[38,39] where the IR absorbance (A) is normalized by d_e. The absorbance A corresponds to the SiO_2 film remaining at any given moment during etching. A is approximated by the sum of two absorbance spectra:

$$A = A_o + A_{\exp}, \tag{1}$$

where A_o is the absorbance spectrum representing the pre-etch SiO_2 film taken with respect to the clean Ge ATR crystal, and $A_{\exp}$ is the experimentally measured absorbance spectrum taken with respect to a pre-etch background where the patterned PR and ARC are stacked on top of yet-to-be-etched SiO_2. A and d_e are related to the extinction coefficient (k) of the mesoporous SiO_2 film by

$$\tilde{k}(\tilde{\nu}) = \frac{A(\tilde{\nu})}{4\pi N_R d_e(\tilde{\nu})}, \tag{2}$$

where $\tilde{\nu}$ and N_R denote the wave number in cm^{-1} and the number of internal reflections from the SiO_2–Ge interface, respectively. N_R is 12 in this case. Since d_e is yet unknown, the pre-etch SiO_2 film thickness is used as the initial value of d_e. k is related to the real part (n) of the complex refractive index ($\tilde{n}=n+ik$) for the SiO_2 film by the Kramers–Kronig dispersion relation:

$$n_i = 1 + \frac{2}{\pi}\left[P\int_0^{\infty} \frac{\tilde{\nu}k(\tilde{\nu})}{\tilde{\nu}^2 - \tilde{\nu}_i^2} d\tilde{\nu}\right], \tag{3}$$

where n_i is the refractive index of the film at wave number $\tilde{\nu}_i$, and P denotes the Cauchy principle value of the integral from zero to infinity. However, the experimentally collected spectrum has a finite wave number range within the mid-IR region, and the integral cannot be evaluated from zero to infinity. This limitation can be circumvented by measuring a real part (n_r) of the complex refractive index at a known wave number $\tilde{\nu}_r$ and subtracting n_r from n_i. The inherent assumption is that the difference between n_i and n_r is close to zero in the domains outside the experimentally accessible wave number range: i.e., $0 \leq \tilde{\nu} < \tilde{\nu}_1$ and $\tilde{\nu}_2 < \tilde{\nu} \leq \infty$. This assumption leads to

$$n_i = n_r + \frac{2}{\pi}\left[P\int_{\tilde{\nu}_i}^{\tilde{\nu}_2} \frac{\tilde{\nu}k(\tilde{\nu})}{\tilde{\nu}^2 - \tilde{\nu}_i^2} d\tilde{\nu} - P\int_{\tilde{\nu}_i}^{\tilde{\nu}_2} \frac{\tilde{\nu}k(\tilde{\nu})}{\tilde{\nu}^2 - \tilde{\nu}_r^2} d\tilde{\nu}\right], \tag{4}$$

where n_r is measured at $\tilde{\nu}_r = 15\,800\ cm^{-1}$ by spectroscopic ellipsometry (SE).[13] The experimentally measured value of n_r is 1.26 for the mesoporous SiO_2 film. The limits ($\tilde{\nu}_1$ and $\tilde{\nu}_2$) of integration in the principle integral are 650 and 4000 cm^{-1}, respectively.

The value of n_i from Eq. (4) is then used to calculate the two components of the evanescent field: $E_{0\parallel}$ that is parallel to the substrate surface and $E_{0\perp}$ that is perpendicular to the substrate surface. The strength of these two components depends on n_i of the mesoporous SiO_2; $n_1(\tilde{\nu})$, the real part of the complex refractive index for Ge ATR crystal; and $n_3(\tilde{\nu})$, the real part of the complex refractive index for vacuum. $n_3(\tilde{\nu})$ approximates the refractive index of high vacuum in the etch chamber. Denoting n_i as $n_2(\tilde{\nu})$ for convenience, $E_{0\parallel}$ is expressed as

$$E_{0\parallel}=\frac{2\cos\theta[(1+n_{32}^4)\sin^2\theta-n_{31}^2]^{1/2}}{(1-n_{31}^2)^{1/2}[(1+n_{31}^2)\sin^2\theta-n_{31}^2]^{1/2}}, \quad (5)$$

where n_{lm} ($l=3$ and $m=1$ or 2) denotes n_l-to-n_m ratio. The perpendicular component, $E_{0\perp}$, is expressed as

$$E_{0\perp}=\frac{2\cos\theta}{(1-n_{31}^2)^{1/2}}. \quad (6)$$

The value of n_i from Eq. (4) is also used to calculate the characteristic penetration depth (d_p) of the evanescent wave by

$$d_p=\frac{\lambda/n_1}{2\pi(\sin^2\theta-n_{21}^2)^{1/2}}, \quad (7)$$

where λ is the IR wavelength in vacuum, and θ is the incident angle of the IR on the top surface inside the ATR crystal. The effective thickness (d_e) is then expressed as

$$d_e=\frac{n_{21}E_0^2}{2\cos\theta}d_p[1-\exp(-2\delta/d_p)], \quad (8)$$

where δ is the remaining SiO_2 film thickness. δ is calculated by

$$\delta=\delta_o-(ER\times t), \quad (9)$$

where δ_o, ER, and t represent pre-etch SiO_2 film thickness, etch rate measured on a blank SiO_2 film, and etch duration, respectively. Since the SiO_2 film is partially masked during the pattern etch, δ is an underestimation of remaining SiO_2. Equation (9) also assumes that the vertical etch rate remains constant throughout etching. To account for possible loading effect and time-dependent etch rate, *in situ* spectroscopic ellipsometry[14,40] or interferometry[41,42] can be used for more reliable estimate on δ. Note that Eq. (8) results in two effective thickness values ($d_{e\parallel}$ and $d_{e\perp}$), depending on whether $E_{0\parallel}$ or $E_{0\perp}$ is used in place of E_0. As an approximation, the arithmetic average of $d_{e\parallel}$ and $d_{e\perp}$ obtained from Eq. (8) is used for d_e in Eq. (2) to calculate k. The above procedure using Eqs. (2)–(8) is repeated until n_i and k converge. To test their convergence, the real part (ε_1) of the complex dielectric constant ($\bar{\varepsilon}$) is first calculated by

$$\varepsilon_1=n^2-k^2, \quad (10)$$

where the subscript i for n_i is omitted for convenience. The imaginary part (ε_2) is then calculated by

$$\varepsilon_2=2nk. \quad (11)$$

The magnitude of $\bar{\varepsilon}$ is then expressed as

$$\bar{\varepsilon}=\sqrt{\varepsilon_1^2+\varepsilon_2^2}. \quad (12)$$

We employ an absolute convergence criterion where the root mean square (rms) value defined in Eq. (13) is less than 10^{-2}:

$$\text{rms}=\sqrt{\sum_k^N(\bar{\varepsilon}_{k,l+1}-\bar{\varepsilon}_{k,l})^2/N}, \quad (13)$$

where k is the kth wave number, l is the lth iteration, and N is the number of experimental data points in the absorbance spectrum.

After d_e is self-consistently calculated by the procedure described above, the absolute amount of SiO_2 remaining at each moment during etching is approximated by

$$N_{\text{Si–O–Si}}=\frac{2.60\times10^{12}\ \text{cm}^{-1}}{N_R}\frac{1}{f}\int_{\tilde{\nu}_1}^{\tilde{\nu}_2}\frac{A_{\text{Si–O–Si}}(\tilde{\nu})d\tilde{\nu}}{d_e(\tilde{\nu})}\times\delta\times A_{\text{top}}, \quad (14)$$

where $N_{\text{Si–O–Si}}$ is the total number of Si–O–Si removed, f is the oscillator strength of Si–O–Si stretching vibrational mode, and A_{top} is the top surface area of the Ge ATR crystal. The integration is evaluated from $\tilde{\nu}_1=984\ \text{cm}^{-1}$ to $\tilde{\nu}_2=1195\ \text{cm}^{-1}$. The top surface area remains constant at 5 cm^2, while δ decreases according to Eq. (9). The oscillator strength is 7.38×10^{-5} calculated from [43]

$$f=1.29\times10^{17}\frac{\alpha W}{N_{\text{mesoporous}}}\frac{n_{\text{IR}}}{(n_{\text{IR}}^2+2)^2}, \quad (15)$$

where α, W, $N_{\text{mesoporous}}$, and n_{IR} denote the peak absorption coefficient (1.72 cm^{-2}), the full width at half maximum (100 cm^{-1}) for the Si–O–Si absorbance band, the concentration of SiO_2 units ($\sim1.92\times10^{22}\ \text{cm}^{-3}$) in the mesoporous film, and the real part (1.84) of the complex refractive index near the 1050 cm^{-1} region. We approximate $N_{\text{mesoporous}}$ by

$$N_{\text{mesoporous}}=\frac{n_{\text{mesoporous}}}{n_{\text{thermal}}}N_{\text{thermal}}, \quad (16)$$

where $n_{\text{mesoporous}}$ and n_{thermal} denote the real part of the complex refractive index in the visible range for mesoporous SiO_2 at 1.26 and that of thermal SiO_2 at 1.46, respectively. The experimentally measured $n_{\text{mesoporous}}$ is identical to a reported value.[36] N_{thermal} is $2.2\times10^{22}\ \text{cm}^{-3}$ based on the specific gravity and molecular weight of thermally grown SiO_2.[44] n_{IR} of mesoporous SiO_2 is similarly approximated to be 1.84 by Eq. (16), based on n_{IR} of thermal SiO_2 at 2.12.

For C–F, the total number of C–F ($N_{\text{C–F}}$) created during etching is calculated from [45]

$$N_{\text{C–F}}=\frac{1}{N_R}\frac{1}{\sigma_{\text{C–F}}}\int_{\tilde{\nu}_1}^{\tilde{\nu}_2}\frac{A_{C-F}(\tilde{\nu})d\tilde{\nu}}{\tilde{\nu}d_e(\tilde{\nu})}\times\delta_{\text{C–F}}\times(ER\times t)\times L, \quad (17)$$

where $\sigma_{\text{C–F}}$ is the IR cross-section of C–F stretching vibrational mode ($2.84\times10^{-20}\ \text{cm}^2$),[46] $\delta_{\text{C–F}}$ is the thickness of the fluorocarbon sidewall passivation, and L is the length of the etched trenches (5 cm). The integration is evaluated from $\tilde{\nu}_1=1200\ \text{cm}^{-1}$ to $\tilde{\nu}_2=1700\ \text{cm}^{-1}$. For comparison purpose only, we assume that $\delta_{\text{C–F}}$ remains constant[32] at 1 nm,[47] contrary to the reported observation that $\delta_{\text{C–F}}$ tapers down towards the bottom of the etched trenches.[31] This assumption helps visualize how the sidewall passivation thickness

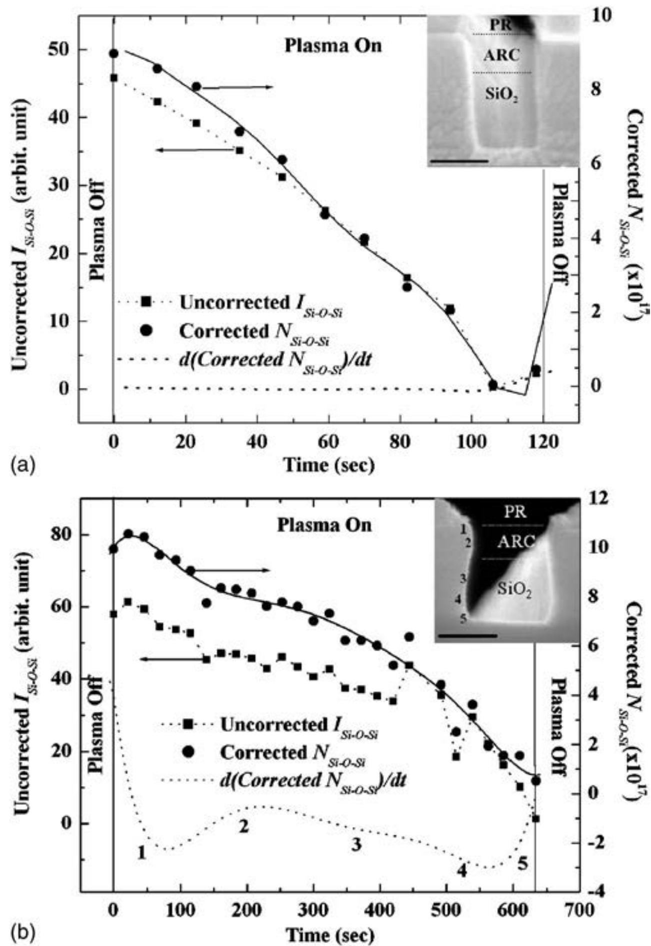

FIG. 4. Integrated absorbance of Si–O–Si is plotted vs time for (a) a sample with relatively anisotropic etch profile and (b) a sample with highly nonideal, bell-jar shaped etch profile. The corresponding cross-sectional SEM images are shown in the insets. The scale bar is 200 nm. The IR absorbance corrected for the exponentially decaying evanescent field is used to calculate the total loss of Si–O–Si bonds. A nonlinear slope of total Si–O–Si loss ($N_{Si-O-Si}$) during plasma-on period foretells a deviation from perfect anisotropy. The nonideal profile is particularly pronounced for the profile shown in (b).

changes as a function of time. If N_{C-F} deviates from a linear line, then the slope of N_{C-F} describes a number of scenarios, as to whether the actual δ_{C-F} tapers down towards the trench bottom, thickens towards the trench bottom, or thickens over the entire passivation layer while maintaining the general tapered down cross-section.

The SEM images in Fig. 4 illustrate two contrasting examples of profile evolution: (a) anisotropic profile and (b) highly nonideal, bell-jar shaped profile. The lateral opening of the SiO_2 trench is ~0.15 μm for both profiles. The CHF_3 and Ar flow rates, rf power to the plasma source, and rf power to the substrate are maintained at 22 and 45 sccm, 800 W, and 150 W, respectively, for the anisotropic profile and at 11 and 50 sccm, 400 W, and 100 W, respectively, for the bell-jar shaped profile. Another difference is that the ARC is etched in an O_2–Ar plasma for 5 min for the anisotropic profile, whereas the ARC is etched under the identical conditions used in SiO_2 etch for the bell-jar shaped profile. The etch is stopped 30 s (~10% overetch) after the presumed endpoint based on the etch rates observed on identically patterned samples. Despite the overetch, we have determined that the underlying Ge etch is below detection limit.

Corresponding to the two etch profiles, Fig. 4 shows the integrated absorbance of Si–O–Si ($I_{Si-O-Si}$) before correcting for the exponentially decaying evanescent wave. $I_{Si-O-Si}$ qualitatively indicates that SiO_2 is removed approximately at a constant rate for the anisotropic profile and at a rate that varies throughout the etch for the bell-jar shaped profile. The detailed quantitative information on profile evolution is extracted from $N_{Si-O-Si}$ based on Eq. (14). $N_{Si-O-Si}$ accounts for the exponential decay, and its time derivative conveys the information on profile evolution. We employ a fifth-order polynomial function (—) to fit $N_{Si-O-Si}$ (●). The smoothness of the polynomial fit reduces the noise in the calculated rate of decrease (---). The rate of decrease is equivalent to the removal rate of SiO_2. The removal rate accounts for both lateral and vertical losses; therefore, the removal rate is different from the blank film etch rate. For instance, the dotted line (---) in Fig. 4(a) indicates that the SiO_2 removal rate remains nearly constant until the very end of the etch process between 100 and 120 s. The reduced removal rate translates to narrowing profile, and the SEM image in Fig. 4(a) shows a slight footing near the bottom of the trench.

For the bell-jar shaped profile in Fig. 4(b), we demonstrate that the profile evolution of ARC and SiO_2 can be successively monitored. To this end, the IR absorbance of characteristic vibrational modes of ARC, which appear in the 1080 cm^{-1} region, is included in the calculation of $N_{Si-O-Si}$. Thus, $N_{Si-O-Si}$ partially reflects the removal rate of ARC in addition to that of SiO_2. The nonlinearity in the ARC and SiO_2 removal rate is consistent with the bulging profile of ARC and the lateral erosion of SiO_2. One can trace Points 1–5 on the removal rate curve (---) and match them with the corresponding points in the SEM image. Note that the removal rate is negative with its corresponding axis on the right hand side. Thus, the absolute removal rate increases with increasingly negative quantity. The observed removal rate suggests that the ARC etching lasts ~350 s, after which SiO_2 etch begins at a comparatively accelerated pace. In Fig. 4(b), $I_{Si-O-Si}$ at 350 s is ~50, matching that of initial $I_{Si-O-Si}$ in Fig. 4(a). Since the SiO_2 thickness of the sample in Fig. 4(a) is the same as that in Fig. 4(b), this equivalence validates the demarcation of when ARC etch ends, and SiO_2 etch begins, while supporting the positional accuracy of assigned numbers (Points 1–5) along the etch profile. In the future, we plan to compare the etch profiles, that are predicted and independently verified by XSEM, with experimentally measured ion energy and angular distribution functions in SiO_2, Si_3N_4, and SiO_xN_y cases where the etch is strongly driven by ion bombardment.

The absolute amount of C–F formation during etching, calculated from the absorbance of C–F stretching vibrational mode by Eq. (17), is shown in Fig. 5. Figure 5(a) corresponds to Fig. 4(a), and Fig. 5(b) corresponds to Fig. 4(b). In contrast to $N_{Si-O-Si}$, N_{C-F} increases throughout the etch. The

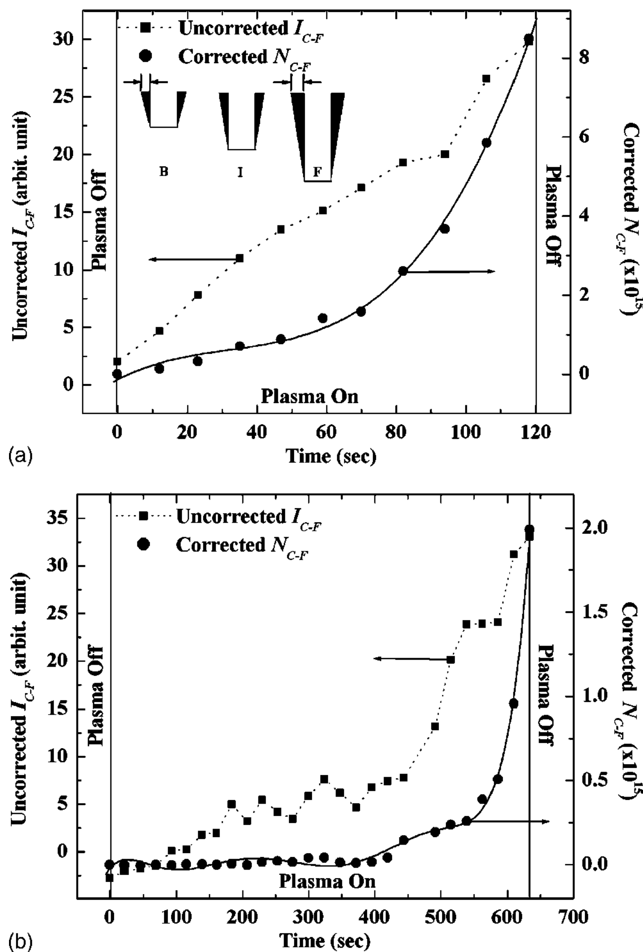

FIG. 5. IR absorbance of C–F stretching vibrational mode near 1300 cm^{-1} corrected for the exponentially decaying evanescent field strength is used to calculate the total number of C–F formed during etching for (a) a sample with relatively anisotropic etch profile and (b) a sample with highly nonideal, bell-jar shaped etch profile. The inset in (a) conceptually describes the shape and thickness of sidewall passivation in the beginning (B), intermediate (I), and final (F) stage of etching. Note that the inset is not drawn to scale. The C–F buildup is pronounced towards the end point, and a critical buildup is necessary to maintain the anisotropic profile.

C–F accumulation rate is calculated from the slope of $N_{\text{C–F}}$, in the same way the SiO_2 removal rate is calculated. The accumulation rate, which rises sharply towards the end of the etching process, suggests that the most of C–F accumulation occurs towards the end, when the trench bottom meets the underlying Ge ATR crystal. If the sidewall passivation profile is assumed to maintain its wedge shape tapering down towards the trench bottom during etching, the sharp rise in $N_{\text{C–F}}$ translates to a profile evolution schematically drawn in the inset of Fig. 5(a). B, I, and F in the inset represent beginning, intermediate, and final stage of etching, respectively. The profile maintains its downward wedge shape, but its overall thickness rises sharply near the endpoint. Both anisotropic and bell-jar shaped samples commonly share this trend. The only dramatic difference between the two samples is the absolute amount of C–F accumulation. The anisotropic profile exhibits a high level of C–F bond accumulation throughout the etch (8×10^{15} total when the etch is complete), whereas the bell-jar shaped profile exhibits a comparatively low level of C–F bond accumulation (2×10^{15} total at the end). Given the same SiO_2 thickness and trench top opening width, we infer that a critical amount of C–F exists, below which a substantial lateral loss in SiO_2 occurs. That is, the sample corresponding to Figs. 4(b) and 5(b) does not have enough fluorocarbon buildup on the sidewalls and, therefore, not enough passivation thickness to prevent the lateral loss.

IV. CONCLUSIONS

We have demonstrated the use of ATR-FTIRS to monitor the etch profile evolution of mesoporous, low-dielectric-constant SiO_2 *in situ* and in real time. The technique is nonintrusive as well as nondestructive, eliminating the necessity to cleave the etched samples for SEM imaging. We rely on the IR absorbance of Si–O–Si stretching vibrational mode during etching to calculate the SiO_2 loss. When the absorbance spectra are corrected for the exponentially decaying strength of the evanescent wave, using the algorithm described in Results and Discussion, the total amount of SiO_2 loss can be monitored in real time, and the removal rate is calculated from the slope of total SiO_2 loss. The calculated removal rate and the corresponding etch profile show good agreement, further validating that the ATR technique can be used to predict the profile evolution during etching. In a similar approach, we have investigated the fluorocarbon accumulation during etching. The total accumulation of C–F and the corresponding profile suggest that a critical amount of C–F buildup is needed to maintain an anisotropic profile and that the most of C–F buildup occurs towards the end of etching.

ACKNOWLEDGMENTS

The authors thank University of New Mexico SEED and the National Science Foundation CAREER (Award Number DMR-0094145) for generous financial support.

[1] International Technology Roadmap for Semiconductors, http://public.itrs.net/Files/2003ITRS/Home2003.htm (2003).
[2] J. Bremmer, Solid State Technol. Suppl. S3 (2001).
[3] S. Takeishi, H. Kudo, R. Shinohara, M. Hoshino, S. Fukuyama, J. Yamaguchi, and M. Yamada, J. Electrochem. Soc. **144**, 1797 (1997).
[4] T. E. F. M. Standaert, P. J. Matsuo, X. Li, G. S. Oehrlein, T. M. Lu, R. Gutmann, C. T. Rosenmayer, J. W. Bartz, J. G. Langan, and W. R. Entley, J. Vac. Sci. Technol. A **19**, 435 (2001).
[5] J. L. Hedrick, K. R. Carter, J. W. Labadie, R. D. Miller, W. Volksen, C. J. Hawker, D. Y. Yoon, T. P. Russell, J. E. McGrath, and R. M. Briber, Adv. Polym. Sci. **141**, 1 (1999).
[6] H. J. Cha, J. Hedrick, R. A. DiPietro, T. Blume, R. Beyers, and D. Y. Yoon, Appl. Phys. Lett. **68**, 1930 (1996).
[7] J. L. Hedrick, R. D. Miller, C. J. Hawker, K. R. Carter, W. Volksen, D. Y. Yoon, and M. Trollsas, Adv. Mater. (Weinheim, Ger.) **10**, 1049 (1998).
[8] C. V. Nguyen, K. R. Carter, C. J. Hawker, J. L. Hedrick, R. L. Jaffe, R. D. Miller, J. F. Remenar, H. W. Rhee, P. M. Rice, M. F. Toney, M. Trollsas, and D. Y. Yoon, Chem. Mater. **11**, 3080 (1999).
[9] C. J. Brinker, Curr. Opin. Solid State Mater. Sci. **1**, 798 (1996).
[10] L. W. Hrubesh, L. E. Keene, and V. R. Latorre, J. Mater. Res. **8**, 1736 (1996).
[11] S. J. Ullal, T. W. Kim, V. Vahedi, and E. S. Aydil, J. Vac. Sci. Technol. A **21**, 589 (2003).
[12] S. M. Han and E. S. Aydil, J. Vac. Sci. Technol. A **14**, 2062 (1996).

[13]S. M. Han and E. S. Aydil, J. Appl. Phys. **83**, 2172 (1997).
[14]D. C. Marra and E. S. Aydil, J. Vac. Sci. Technol. A **15**, 2508 (1997).
[15]S. J. Ullal, H. Singh, J. Daugherty, V. Vahedi, and E. S. Aydil, J. Vac. Sci. Technol. A **20**, 1195 (2002).
[16]Z. Zhou, E. S. Aydil, R. A. Gottscho, Y. J. Chabal, and R. Reif, J. Electrochem. Soc. **140**, 3316 (1993).
[17]S. M. Han and E. S. Aydil, J. Vac. Sci. Technol. A **14**, 2062 (1996).
[18]J. R. Woodworth, I. C. Abraham, M. E. Riley, P. A. Miller, T. W. Hamilton, B. P. Aragon, and C. G. Willison, J. Vac. Sci. Technol. A **20**, 873 (2002).
[19]R. J. Hoekstra and M. J. Kushner, J. Appl. Phys. **79**, 2275 (1996).
[20]J. R. Woodworth, M. E. Riley, D. C. Meister, B. P. Aragon, M. S. Le, and H. H. Sawin, J. Appl. Phys. **80**, 1304 (1996).
[21]R. A. Gottscho, J. Vac. Sci. Technol. B **11**, 1884 (1993).
[22]H. Gerung, D. Doshi, C. J. Brinker, and S. M. Han, AVS 49th International Symposium, Denver, CO (2002).
[23]K. Ishikawa and M. Sekine, J. Appl. Phys. **91**, 1661 (2002).
[24]C. T Kirk, Phys. Rev. B **38**, 1255 (1988).
[25]C. J. Brinker and G. W. Scherer, *Sol-Gel Science*, 1st ed. (Academic, San Diego, 1990), pp. 108–216.
[26]C. J. Brinker, Y. F. Lu, A. Sellinger, and H. Y. Fan, Adv. Mater. (Weinheim, Ger.) **11**, 579 (1999).
[27]X. L. Chen and S. R. J. Brueck, Opt. Lett. **24**, 124 (1999).
[28]S. H. Zaidi and S. R. J. Brueck, J. Vac. Sci. Technol. B **11**, 658 (1993).
[29]E. H. Anderson, C. M. Horwitz, and H. I. Smith, Appl. Phys. Lett. **43**, 874 (1983).
[30]L. F. Johnson, G. W. Kammlott, and K. A. Ingersoll, Appl. Opt. **17**, 1165 (1978).
[31]G. S. Oehrlein and Y. Kurogi, Mater. Sci. Eng., R. **24**, 153 (1998).
[32]A. Sankaran and M. J. Kushner, Appl. Phys. Lett. **82**, 1824 (2003).
[33]N. R. Rueger, J. J. Beulens, M. Schaepkens, M. F. Doemling, J. M. Mirza, T. E. F. M. Standaert, and G. S. Oehrlein, J. Vac. Sci. Technol. A **15**, 1881 (1997).
[34]T. E. F. M. Standaert, C. Hedlund, E. A. Joseph, G. S. Oehrlein, and T. J. Dalton, J. Vac. Sci. Technol. A **22**(1), 53 (2004).
[35]E. Gogolides, P. Vauvert, G. Kokkoris, G. Turban, and A. G. Boudouvis, J. Appl. Phys. **88**, 5570 (2000).
[36]T. E. F. M. Standaert, E. A. Joseph, G. S. Oehrlein, A. Jain, W. N. Gill, P. C. Wayner, Jr., and J. L. Plawsky, J. Vac. Sci. Technol. A **18**, 2742 (2000).
[37]S. M. Han and E. S. Aydil, J. Electrochem. Soc. **144**, 3963 (1997).
[38]N. J. Harrick, *Internal Reflection Spectroscopy*, 1st ed. (Wiley, New York, 1967), p. 42.
[39]F. M. Mirabella, Jr., in *Internal Reflection Spectroscopy*, 1st ed. (Marcel Dekker, New York, 1993), p. 17.
[40]W. M. Duncan and S. A. Henck, Appl. Surf. Sci. **63**, 9 (1993).
[41]T. J. Dalton, W. T. Conner, and H. H. Sawin, J. Electrochem. Soc. **141**, 1893 (1994).
[42]D. Economou, E. S. Aydil, and G. Barna, Solid State Technol. **34**, 107 (1991).
[43]K. Awazu, J. Non-Cryst. Solids **260**, 242 (1999).
[44]W. R. Runyan and K. E. Bean, *Semiconductor Integrated Circuit Processing Technology* (Addison-Wesley, New York, 1990), p. 58.
[45]M. H. Brodsky, M. Cardona, and J. J. Cuomo, Phys. Rev. B **16**, 3556 (1977).
[46]X. Wang, H. Harris, H. Temkin, S. Gangopadhyay, M. D. Strathman, and M. West, Appl. Phys. Lett. **78**, 3079 (2001).
[47]T. E. F. M. Standaert, M. Schaepkens, N. R. Rueger, P. G. M. Sebel, G. S. Oehrlein, and J. M. Cook, J. Vac. Sci. Technol. A **16**, 239 (1998).